

Feb. 14, 2011

Revision 2

-submitted to the Journal of Geophysical Research - Space Physics

**Temporal Properties of Terrestrial Gamma-ray Flashes (TGFs)
from the
Gamma-ray Burst Monitor on the Fermi Observatory**

G. J. Fishman¹, M.S. Briggs², V. Connaughton², P. N. Bhat², W. S. Paciasas²,
A. von Kienlin³, C. Wilson-Hodge¹, R. M. Kippen⁴, R. Preece²,
C. A. Meegan⁵ and J. Greiner³

1. Space Science Office, VP62, NASA-Marshall Space Flight Center, Huntsville, AL 35812
USA jerry.fishman@msfc.nasa.gov
2. University of Alabama in Huntsville, Huntsville, AL 35805 USA
3. Max Plank Institute for Extraterrestrial Physics, Garching, Germany
4. Los Alamos National Laboratory, Los Alamos, NM USA 87545
5. Universities Space Research Association, Huntsville, AL USA 35805

Abstract

The Gamma-ray Burst Monitor (GBM) on the Fermi Gamma-ray Space Telescope (Fermi) detected 50 terrestrial gamma-ray flashes (TGFs) during its first 20 months of operation. The high efficiency and large area of the GBM detectors, combined with its fine timing capabilities and relatively high throughput, allows unprecedented studies of the temporal properties of TGFs. The TGF pulses are observed to have durations as brief as ~ 0.05 ms, shorter than previously measured. There is a relatively narrow distribution of pulse durations; the majority of pulses have total durations between 0.10 ms and 0.40 ms. In some TGF events, risetimes as short as ~ 0.01 ms and falltimes as short as ~ 0.03 ms are observed. Three of the 50 TGFs presented here have well-separated, double peaks. Perhaps as many as ten other TGFs show evidence, to varying degrees, for overlapping peaks. Weak emission is seen at the leading or trailing edges of some events. There are five of the 50 TGFs that are considerably longer than usual; these are believed to be caused by incident electrons transported from a TGF at the geomagnetic conjugate point. TGF temporal properties can be used to discriminate between models of the origin of TGFs and also provide some basic physical properties of the TGF process.

1. Introduction

The phenomenon of Terrestrial Gamma-ray Flashes (TGFs), brief flashes of MeV photons above thunderstorms, is of great current interest. There appears to be a general consensus that the TGF mechanism results from a “runaway” electron process within strong electric fields associated with thunderstorms. This field accelerates electrons to high energies, producing an avalanche and forming an intense, relativistic electron beam. The resulting beam produces x-rays and gamma-rays via the bremsstrahlung process in the residual atmosphere. A combined electron, positron, and photon shower ensues until it emerges from the upper atmosphere. There are numerous theoretical papers and numerical simulations which give details of this process (e.g. Gurevich et al., 1992, 1999, 2004, 2007; Roussel-Dupré and Gurevich, 1996; Roussel-Dupré et al., 1998; Lehtinen et al., 1996, 1999; Taranenko and Roussel-Dupré, 1996; Gurevich and Zybin, 2005; Babich et al., 2007, 2008; Carlson et al., 2007, 2008, 2010; Ostgaard et al., 2008; Chang et al., 2005; Dwyer and Smith, 2005; Dwyer 2008; Inan and Lehtinen, 2005; Inan et al., 2006; Milikh et al., 2005; Williams et al., 2006; Shao et al. 2010, and references therein). A succinct overview of the current state of TGF theory and modeling, along with a summary of past TGF observations is given in the introduction of the paper by Grefenstette et al. (2009). Additional, recent observations of TGFs have been made with the Italian satellite “AGILE” (Marisaldi et al., 2010a,b; Tavani 2011).

In spite of extensive modeling and simulations, some basic properties of TGFs remain unanswered by direct observations. These include: the intensity distribution of TGFs and

their lower limit of intensity or threshold of occurrence, if any; the altitude range of the origin of the emission; the cutoff energy, variations of TGF spectra at the source; the beaming characteristics of the radiation; the type(s) of lightning that are associated with the production of TGFs, and the temporal relationships of TGFs to the lightning associated with them. The latter was first examined by Inan et al. (1996) and more recently in papers by Cummer et al., 2005; Stanley et al., 2006; Lu et al., 2010; Cohen, et al., 2010; Briggs et al., 2010, and Connaughton, et al., 2010.

TGFs have now been detected with four different orbiting spacecraft. The observations reported here were made with the Gamma-ray Burst Monitor (GBM) scintillation detectors of the Fermi Gamma-ray Space Telescope (Fermi). Observations of TGFs were first made with the BATSE experiment on the Compton Gamma-ray Observatory (Fishman et al, 1994). They have subsequently been observed with the Ramaty High-Energy Solar Spectroscopy Explorer, RHESSI (Smith et al., 2005; Grefenstette et al., 2009), and the Italian gamma-ray astronomy spacecraft “AGILE” (Fuschino, et al. 2009; Marisaldi et al., 2010a, 2010b.). Gamma-ray emission has also been reported from ground observations of rocket-triggered lightning (Dwyer 2004). Space-borne observations of TGFs have not been ideal since they have been made with detectors that have been optimized for other purposes (typically at lower photon energies) and they have been made at a considerable distance. In several experiments, intervening materials have prevented observations of low energy gamma rays from the Earth. The instrument electronics systems are usually not well suited for TGF observations; in order to observe TGFs well, detectors need to have fast timing and immunity to deadtime and pulse pile-

up. Finally, most space-borne gamma-ray detectors do not have good detection efficiency for the high-energy photons of typical TGFs.

The Fermi Gamma-Ray Space Telescope (Fermi, known previously as GLAST) was launched from the Kennedy Space Center on 11 June 2008, into a nearly circular orbit with an altitude of ~560 km and an inclination of 25.6 degrees. The GBM detector system on Fermi is observing TGFs in more detail than previous TGF-observing detector systems. The GBM detectors have high detection efficiency over a broad energy range. Although GBM has been observing TGFs less frequently than the RHESSI spacecraft due to the requirement of an on-board trigger for data accumulation, its larger effective area allows higher precision temporal observations to be made on those TGFs that trigger the onboard data system. Instead of an on-board trigger, RHESSI transmits the complete set of time- and energy-tagged counts, and TGFs are detected post-facto by analysis of data on the ground, which allows much weaker TGFs to be recorded. A similar detection method has been recently implemented for the GBM experiment over a limited portion of its orbit, however TGFs detected by that means are still undergoing analysis and are not presented here. This method of TGF detection is expected to enable the detection of more numerous, weaker TGFs that are now being missed due to the on-board trigger requirement of GBM.

The primary objective of the GBM instrument is the study of cosmic gamma-ray bursts (GRBs). To accomplish this, the GBM detectors autonomously “trigger” on GRBs by continuously monitoring the counting rate of the detectors and comparing them to the

prior background. The instrument does this on various time scales and in different energy bands; these can be modified in the flight software. Since GRBs are known to emit most photons in the energy band ~ 30 keV to ~ 1 MeV, the trigger energy windows were set within these energy limits, using only the NaI detectors.

The GBM detector system became operational on 11 July 2008, after the detectors were turned on and the on-board trigger system was enabled. With the initial on-board trigger requirements, the Fermi-GBM instrument was detecting on the average about one TGF per month (Figure 1). On 10 November 2009, the GBM trigger algorithms were modified so that triggers could be obtained at the higher energies typical of TGFs through the use of data from the high energy detectors in the triggering algorithms (the BGO detectors, described below). This change has resulted in an increase in the GBM trigger rate by a factor of ~ 8 , to about two per week. Of the 50 TGFs presented here, 35 of these occurred following this change to the flight software which enabled the higher detection efficiency.

This paper follows an initial paper published recently on the first observations of TGFs with Fermi-GBM (Briggs et al., 2010). That paper described some properties of the first 12 TGFs observed from GBM. It also gave more details of the instrument, details of the effects of pulse pile-up and deadtime in the observations, and showed several functional fits to the observed TGF pulses. A discussion was presented of the corrections to deadtime that are needed, the use of a deconvolution method used to estimate the peak flux and the assumptions and uncertainties associated with these corrections. It also

described how cosmic-ray showers in the spacecraft could be misidentified as TGFs and the means by which they are separated. These aspects of GBM and the GBM-observed TGFs will not be repeated in this paper.

We report here on the observed temporal properties of a considerably larger sample of TGFs observed with GBM. The high time resolution data from this larger sample better indicates that there are several distinct categories of TGFs that can be identified solely by their time profiles. These results also show that the durations of a majority of TGFs are considerably shorter than has been previously thought. Although spectral studies of the TGFs are still in progress and are not reported in this paper, those observations may also eventually aid in the categorization and study of TGFs.

2. GBM Instrument and Triggering Requirements

The GBM experiment comprises two different types of scintillation detectors, Sodium Iodide (NaI) and Bismuth Germanate (BGO). Details of the experiment are described in a comprehensive paper (Meegan et al., 2009) and in (Briggs et al., 2010). Even though the GBM experiment was designed and optimized for the observation of cosmic gamma-ray bursts (GRBs), it has also unprecedented capabilities for TGF observations. The thick bismuth germanate (BGO) scintillation detectors of the GBM system have observed photon energies from TGFs above 35 MeV.

There are twelve NaI detectors on the spacecraft and two BGO detectors. Three NaI detectors are located at each of the four corners of the Fermi Observatory, with axes pointed in different directions (Meegan et al., 2009). The two BGO detectors are placed on opposite sides of the spacecraft. The detectors are unshielded and uncollimated. The on-orbit background counting rates, the orbital variations and spectral characteristics of the background are also described in (Meegan et al., 2009).

The NaI detectors measure the low-energy x-ray and gamma-ray spectral region, from ~ 8 keV to ~ 1 MeV. These scintillation crystal disks have a diameter of 12.7 cm (5 in.) and a thickness of 1.27 cm (0.5 in.). The BGO detector crystals have a diameter of 12.7 cm (5 in.) and a thickness of 12.7 cm (5 in.). They cover an energy range of ~ 100 keV to ~ 45 MeV. The use of two PMTs on the BGO detectors results in better light collection and provides redundancy. Together, the two detector types provide an overlapping, all-sky monitoring capability over a broad energy range. Details of the performance of the GBM detectors are described in Bissaldi et al. (2009) and in Meegan et al. (2009).

The pulse signals from the photomultiplier tubes (PMTs) of the scintillation detectors undergo pulse shaping at the output of the PMTs with a time constant of ~ 0.2 μ s. The shaped pulses from all fourteen detectors are sent to a central Data Processing Unit (DPU) where they are digitized by individual analog-to-digital converters. Signals from all detectors are processed independently, undergoing pulse height analysis where they are sorted into one of 4096 energy channels. These channels are then mapped into several data types via programmable look-up tables (LUTs).

The data type used for the TGF events are called “time-tagged events” (TTE), in which each detected count is assigned to one of 128 energy channels and is tagged with its time-of-arrival to the nearest $2\mu\text{s}$ from an internal clock. The data system is further described in Meegan et al. (2009). The TTE data are continuously recorded in an over-writing, circulating memory. GBM, like BATSE (and unlike RHESSI), requires an on-board trigger to detect a pre-defined, statistically significant rate increase and subsequently store these data. This trigger can occur from any of numerous pre-specified algorithms that are based on combinations on various energy and time windows, and from different combinations of detectors. All of these trigger detection algorithms operate simultaneously. The end of a time window that triggers the first algorithm that has met its trigger conditions is defined as the “trigger time”. Due to on-board hardware limitations, the minimum time window for a GBM trigger is 16 ms. This greatly reduces the number of detected TGFs, since nearly all TGFs that have been detected so far have a much shorter duration than this window. Thus background counts from various sources, e.g. cosmic rays, radioactivity, etc., within this relatively long trigger window are included in most trigger determinations (see Figure 2). However, those TGFs that do manage to trigger on this timescale have a very high signal-to-background during the brief time of the TGF. In contrast, the minimum BATSE trigger time window was 64 ms (Fishman et al., 1994). The AGILE detector system has operated at various trigger timescales, some as short as 0.293 ms (Marisaldi et al., 2010a).

Until 10 November 2009, only data from the lower-energy-responding NaI detectors were used in all of the GBM on-board trigger algorithms. This was highly inefficient for the detection of TGFs because the TGFs have a much harder spectrum than the background radiation and the BGO detectors have a high efficiency for the higher energy radiation of the TGFs. The TGF trigger rate increased significantly after the trigger algorithm was changed, as mentioned in Section 1. This is shown in Figure 1.

Figure 2 shows the background radiation of both types of detectors, as well as the signature of a TGF in the GBM detectors in a small sample (150 ms) of data. In both detector types the background spectrum is dominated by lower energy counts. The primary reason that the BGO detectors show a smaller count rate than the NaI detectors is that there are only two of them and their lower energy threshold energy is higher than that of the 12 NaI detectors. The large number of counts shown in Figure 2 near Channel 127 is the “overflow” channel, an integral channel (rather than differential channel) representing the highest energy losses that can be recorded in the detectors. This energy is ~ 1 MeV in the NaI detectors and ~ 43 MeV in the BGO detectors. The presence of a TGF (#7; see Tables 1 and 2) in this section of data is clearly apparent in both detector types at a time of -10.31 ms relative to the trigger time.

3. Detector Response to Gamma-rays; Deadtime and Pulse Pile-up Effects

Above several hundred keV, the dominant interaction of photons with the detector crystal is Compton scattering, resulting in only a partial loss of energy of the gamma-ray photon in the scintillation detectors. At still higher energies (above several MeV), pair production is the dominant interaction. The fraction of total photon energy absorption in the crystal continues to decrease with increasing energy. For the BGO detectors, above ~ 13 MeV the efficiency for detecting the full energy of the incident photon (usually referred to as the photopeak) falls below 50%, resulting in an effective area of ~ 65 cm² (depending somewhat on the incidence angle), for total photon absorption in each BGO detector. For this reason, we refer to “counts” rather than photons (or gamma rays) as the detected data events in this paper. In order to derive a true photon spectrum, a model-dependent deconvolution process is required. This deconvolution process and the spectra of GBM-observed TGFs are not addressed in this paper.

The deadtime per detected count is nominally 2.6 μ s, however in the highest energy channel (the overflow channel) the dead-time was set in the electronics to be 10.4 μ s. This was done in order to allow the analog electronics baseline to be restored following a very large energy deposit in the scintillation crystal. During the brief time of the TGFs, extremely high counting rates are often encountered during portions of many of them. In order to meet their intended objectives for astrophysical observations, the GBM detectors were designed to operate up to rates of ~ 100 kcps (cps = counts per second) from each detector and ~ 500 kcps from the sum of all detectors. The rates during portions of most TGFs observed often exceed these rates, and on occasion extend to several Mcps. These high rates require considerable corrections (with inherent assumptions) to the observed

data in order to derive the true counting rates. A deadtime analysis of a bright TGF (#3) using a deconvolution method estimated that GBM recorded only half of the photons incident on the BGO detectors and 40% during the peak $40 \mu\text{s}$ (Briggs et al., 2010). Thus, absolute count rates and integrated counts from these TGFs are known to be underestimated in the data presented herein. In spite of these limitations in deriving accurate absolute detector count rates, the time profiles presented here, along with the descriptions of their properties such as pulse shapes, durations, and rise-times are still useful for describing previously unobserved properties of TGFs.

4. TGF Temporal Properties Observed with GBM

A list of the first 50 TGFs observed with the GBM instrument in nearly two years of operation are given in Table 1. For GBM data, the triggers are identified by their year (since 2000), month, day, and decimal day (the latter truncated to three decimal places). The absolute time of the trigger is given to the nearest $2 \mu\text{s}$. This time is believed to be accurate to $\sim 20 \mu\text{s}$ and correctable to $\sim 3 \mu\text{s}$, by means of an onboard GPS receiver. Since the point of origin of each TGF has a considerable uncertainty, in Table 1 only the position (the latitude and longitude) of the sub-spacecraft point and the altitude of the spacecraft are given at the time of the trigger. The origin of most TGFs is believed to be within $\sim 300 \text{ km}$ of the sub-spacecraft point (Connaughton et al., 2010; Marisaldi et al., 2010b); gamma rays originating more distant than this would be heavily attenuated, assuming a tropospheric origin. Beaming of the radiation process is also likely to be a

factor in an origin of TGFs relatively near to the sub-satellite point. The locations of these 50 TGFs are mapped in Figure 3. The global distribution of these TGFs is found to be in general agreement with the global distribution of RHESSI TGFs (Grefenstette et al., 2009; Splitt et al., 2010; Smith et al., 2010) and they correspond with the global lightning distribution recorded from the Optical Transient Detector (OTD) and the Lightning Imaging Sensor (LIS) instrument on the TRMM spacecraft (Christian et al., 2003; NASA/MSFC-LIS Data Archive), although a detailed comparison has not yet been made.

A column of Table 1 gives the local solar time in hours and minutes at the location directly beneath the spacecraft (i.e. the time after local midnight). The distribution of the local solar times is shown in Figure 4. The expected correlation between the time of TGFs and thunderstorms is apparent. Of the 50 TGFs observed, there were only 17 TGFs that occurred between local midnight and noon and whereas 33 occurred between noon and midnight. These data are consistent with the local solar time distribution of TGFs described by Splitt et al. (2010), using the more comprehensive dataset from the RHESSI spacecraft. It is interesting to note that they also found a deep minimum of TGFs (with much higher statistical accuracy than that shown in Figure 6) at local solar times between 10^h and 12^h.

Detailed properties of the TGF pulses are given in Table 2. Since three of the TGFs were clearly double pulses (see below), a total of 53 well-separated, individual TGF pulses are treated separately in Table 2. In this table, the TGF pulse durations and the total counts in the pulse are shown. The duration measures t_{50} and t_{90} are common measures used in

gamma-ray burst (GRB) observations. The t_{50} measure is the duration from 25% to 75% (i.e. the central 50%) of the total number of counts detected during the event. Because the peakedness of the profiles is underestimated by the omission of deadtime correction, the t_{50} values are overestimates; they should be considered as upper limits. This is found to be nearly the same as the full-width, half-maximum (FWHM) duration measure, i.e. the pulse width measured distance of half of the height of the peak. Both of these measures contain the majority of the observed fluence (integrated flux) of a pulse. Note that in this paper we have used this t_{50} measure as the TGF pulse duration variable rather than the t_{90} measure used in the Briggs, et al (2010) paper. An estimate of the error of the t_{50} measure in the more intense, shorter duration (<1 ms) TGFs in Table 2 is of the order ~ 20 μ s to ~ 30 μ s. The weaker TGFs have a t_{50} measure uncertainty of ~ 100 μ s. It was found that the TGF duration distribution based on t_{90} was greatly skewed to higher values by TGFs that had weak emission before and after the main period of high emission in the central region. The few number of counts in the leading and trailing 5% of the total counts of many pulses leads to large statistical uncertainties, so that many had abnormally high t_{90} values relative to the t_{50} values. The average ratio of the t_{90} to t_{50} values is: $R_{90/50} = t_{90} / t_{50} = 2.48$, with 12 pulses having $R_{90/50} > 3.0$ and 4 pulses having $R_{90/50} > 3.5$, whereas the expected average should be $R_{90/50} \sim 2.0$, depending somewhat on the assumed pulse shape. For these reasons, we chose to have the duration measure based on t_{50} rather than t_{90} . All detectors are included in the duration determination, except in the case of TGF #1 where a significant signal was registered only in the detectors on one side of the spacecraft. The t_{50} measures of the 53 TGF pulses are given in Table 2. The integrated flux intensity (fluence or total counts) within the t_{50} measure

is also given in Table 2. This measure is greatly reduced due to pulse pile-up and deadtime as described above, especially for the higher intensity pulses, and thus it is only a lower limit to the actual intensity. The detector efficiency is also highly energy-dependent and is quite different for the NaI and BGO detectors. A rough estimate of the total effective area for detecting counts from a TGF, averaged over a full TGF spectrum, for the sum of all detectors is $\sim 700 \text{ cm}^2$, not taking into account deadtime and pile-up. This effective area is greatly dependent upon the incidence angle of the radiation, its spectrum and the amount of intervening materials.

The time profiles of all 53 pulses (Table 2), contained within the 50 TGFs in Table 1, are shown in the 53 sub-figures of Figure 5. In these sub-figures, all TGF pulses are plotted on the same vertical and horizontal scales so they can be directly compared. A bin width of $10 \mu\text{s}$ was chosen to be the finest reasonable bin size that still had meaningful statistics. The full scale of each sub-plot is thirty counts per bin. The plots of Figure 5 are shown over a total time span of 1 ms (100 bins), centered near the peak of the pulse. There are nine weak TGFs that were re-binned to $40 \mu\text{s}$ per bin over a 4 ms time span in order to provide improved statistics and a clearer profile of the TGF. These are shown in Figure 6. For five longer pulses, (#1, #10, #14, #24, and #49), only the initial 1 ms of the entire pulse is shown; the complete pulses, on the appropriate scales covering the entire pulse, are plotted in Figure 7. These five events are believed to be due to incident electrons that originate from a TGF geomagnetically connected to the location of the spacecraft. Such events have been reported previously from BATSE observations of TGFs (Dwyer et al., 2008) and in recent GBM observations (Connaughton et al., 2010; Cohen et al., 2010). In the recent GBM observations, Connaughton et al. (2010) report a lack of lightning

activity at the spacecraft nadir for three of the five longer pulses, with lightning activity at one of the magnetic footprints from which the electron event is believed to originate.

Cohen et al. (2010) associate a particular electric discharge from a storm at the magnetic footprint of Fermi for a long TGF that was detected after the end of the sample presented here. Together, these results suggest an origin for longer TGFs of storms quite distant from the spacecraft nadir, and it is likely that electrons traveling along the field line are the explanation for their detection by GBM. In at least three of these longer events, there is clear evidence for the existence of positrons in the beam in addition to electrons (Briggs et al. 2011).

The proportion of electron events relative to gamma-ray TGFs over the duration of the catalog (10%) is higher than predicted by Dwyer et al. (2008) and Carlson et al. (2009b). Three of these were detected before the flight software change in November 2009, out of a total 15 TGFs. The GBM flight software change made detection of events with fewer counts more probable. Since then, only two new electron events were seen, out of a total 35 new TGFs. This suggests a constant electron TGF rate over the duration of the catalog but a declining proportion of electron TGFs now that the detection threshold is lower. A 16 ms triggering window is more sensitive to events lasting a few ms than to gamma-ray TGFs which are shorter, but with the lower trigger threshold, GBM is now detecting the weaker short events but no new electron events that would not have been detected with the old configuration. The high electron TGF rate is, therefore, a result of the 16 ms triggering window rather than a true measure of the intrinsic electron

to gamma-ray TGF ratio. Further details of GBM electron events will be reported in a future paper.

Three double-pulsed TGFs: #6, #12, and #26, are plotted in Figure 8, with coarse time bins and longer time spans, in order to show their relative intensities and separations. The two peaks of these three TGFs are separated by 1.3 ms, 8.4 ms, and 1.4 ms, respectively. Multiple-pulse TGFs have been observed previously with the BATSE detectors (Fishman et al., 1994; Gjesteland et al., 2010), the RHESSI detectors (Smith et al., 2005; Grefenstette et al., 2009), and the AGILE detectors (Marisaldi et al., 2009). Their cause is unknown. The triggering of GBM TGFs is observationally biased toward multiple-pulsed events, if the pulses occur within the triggering window. This was also true of the TGFs observed with BATSE (Fishman et al., 1994; Grefenstette et al., 2009), where the instrument had even a wider trigger window, 64 ms. Additional details of the time profiles of these plots of TGF pulses are given in the figure captions.

In addition to the three clear double-pulse TGFs, other TGF pulses likely consist of partially overlapping pulses within the main pulse. This was described in Briggs et al., (2010). That paper introduced an analytical pulse fitting procedure that quantified the pulse shapes in order to identify overlapping pulses. Three of the more obvious of these are TGFs #11, #12b, and #13, shown in Figure 9. The time separations of these fitted pulses are: 0.30 ms, 0.30 ms and 0.45 ms, respectively. The possibility of three or more overlapping pulses within a single TGF pulse was not previously considered and is not apparent here. There are other pulses that appear to be unusually broad and may be composed of two (or more) very close, unresolved pulses. There are a total of ~10

possibilities of overlapping pulses in the 53 pulses considered in this paper. The confidence of the separation into overlapping peaks is determined by the peak separation, the ratio of the peak heights, and the statistical significance of the sub-peaks. Other TGF pulses, including the nine weak ones in Figure 7, do not have sufficient counts to attempt a meaningful separation into overlapping pulses. There are other cases (for example TGFs #22, #26a, #27, and #36) that appear to have weak “tails”. In one instance (TGF #23) there appears to be weak emission before the main peak. Alternatively, this emission can be due to a leading weak, unresolved peak.

5. Count Distributions among Individual GBM detectors

For each of the 50 TGFs that are presented in this catalog, only one of them (TGF #1) clearly shows significant differences in the observed count rates among the detectors. This may be due to the fact that this TGF has a softer spectrum than the others, having been identified as an electron event. However, the lack of significant anisotropy in the other electron events is puzzling; it may be due to the spiraling geometry of the incoming electrons. The highly penetrating nature of the high-energy gamma-ray photons of TGFs results in minimal attenuation of the photon flux through the rear of the detectors and through the spacecraft. Unfortunately, the location of the TGFs with respect to the spacecraft position is not determined for most TGFs and the above hypothesis cannot be tested rigorously. This also adds a further complication to the accurate deconvolution (sometimes termed “unfolding”) of the incident TGF energy spectra.

Figure 10 shows the count rates over a 20 ms time span for all 14 Fermi detectors for two TGFs (#1 and #5). The anisotropy in the response of the detectors to TGF #1 is apparent (Figure 10, top), as the detectors on one side of the spacecraft respond with much higher rates than those on the opposite side. The detectors that are all on the same side are detectors NaI #0 through NaI #5 and BGO #0. On the other hand, for TGF #5 (Figure 10, bottom), all detectors of each type respond nearly uniformly. For the highly penetrating gamma-rays from TGFs, the usual methods of locating a source direction by comparison of the Fermi-GBM detector rates are ineffective. Nearly all of the TGFs observed with GBM thus far fall into this latter category.

6. Discussion

Of the 53 pulses listed in Table 2 and shown in Figure 5, if the five long “electron” pulses are treated as a separate phenomenon, then the remaining 48 TGF pulses have a narrow duration distribution that is considerably less than that typically quoted for TGFs. This reinforces the conclusions of Briggs et al. (2010). The t_{50} duration distribution of these 48 pulses were sorted into 11 equal, logarithmically-spaced groups as given in Table 3 and plotted in Figure 11. If we assume that the total pulse duration is $\sim 2xt_{50}$, then the median pulse duration of these 48 TGF pulses is 0.24 ms. If the probable and possible overlapping pulses are not included, then the remaining 38 pulses have a median duration of 0.22 ms. The response of the BATSE instrument on the Compton Gamma Ray

Observatory to high counting rates was not as well characterized as that for GBM. In spite of this, Gjestland et al. (2010) made an estimate of typical BATSE TGF pulses by modeling a significant instrumental deadtime using Monte Carlo methods in order to obtain the true BATSE TGF counting rates and pulse duration. It was found that the average corrected BATSE TGF pulse durations is similar to that of GBM although many of the GBM pulses are measured to be considerably less than half of the mean value. This was not the case in the BATSE simulations. Nemiroff et al. (1997) performed an uncorrected, subjective evaluation of the BATSE TGF durations. These durations were much longer, at least >0.7 ms, and extending to durations considerable higher than this. The rate of multiple peaks in the GBM data presented here was comparable to that found by Gjestland et al. (2010), although the statistics were limited for multiple-peak TGFs.

Some general statements can be made regarding the extremely short values of the risetimes and falltimes observed in most TGFs. Figure 12 shows a selection of six intense, short TGFs that are seen to be very brief, with fast risetimes and falltimes. These are binned with $4 \mu\text{s}$ bins, in order to show these extremely fast risetimes and falltimes, never before observed in TGFs. The fastest risetimes ($1/e$) of these narrow pulses are $\sim 10 \mu\text{s}$, and the fastest falltimes are $\sim 20 \mu\text{s}$. Somewhat surprisingly, many of these fast pulses, as well as many TGFs in Figure 5, appear to be symmetric. (As described above, the count rates near the peak of these pulses are known to have high deadtime, so that the peak rates and the total counts of these fast pulses are underestimated.) With the exception of the five electron TGFs, almost all of the TGF pulses have rise-times less than $\sim 60 \mu\text{s}$ and fall-times from $\sim 80 \mu\text{s}$ to $\sim 400 \mu\text{s}$. Briggs, et

al. (2010) found that in one case (TGF #6b) a risetime of $\sim 7 \mu\text{s}$ was consistent with the data.

As described above, there are four TGFs that have indications of a small, but possibly significant number of counts in “tails” at the trailing end of the main pulse. At least three others (#29, #32, and #39) may also fall into this group. These tails may be due to weak, unresolved pulses or to the possible detection of Compton-scattered photons at the end of the TGF. If they are due to the latter, then these events could have an unusually large number of scattered photons relative to the other TGFs, which would indicate a larger pathlength through the atmosphere, and they would have softer spectra. Preliminary studies of this are inconclusive; we intend to perform more detailed spectral studies of the counts in these tails.

Because of the high temporal resolution and good counting statistics for individual TGFs, we believe that for the first time it is possible to separate observed TGFs into one of only a few TGF categories, as follows: Type I TGFs (the majority of TGFs) have a single, sharp peak, with a relatively narrow duration distribution (FWHM) of between $\sim 50 \mu\text{s}$ and $\sim 200 \mu\text{s}$. (Note that within a duration of $50 \mu\text{s}$, there is only ~ 1 count of background in this interval from the sum of all GBM detectors, so that all short-duration TGF pulses measured with the GBM detectors have a very high signal-to-background ratio.) In TGFs with durations $< 100 \mu\text{s}$, a small percentage ($\sim 15\%$) of the stronger of these show a trailing, weak “tail”, having $\sim 10\%$ of the counts of the main pulse. It is possible that the

weaker Type I TGFs also have these extended tails, however the tails would not be statistically significant in the data.

Of the longer duration TGF pulses, many of them might be attributed to overlapping Type I pulses (as shown in Figure 11), each sub-pulse having a duration $< \sim 100 \mu\text{s}$. A TGF that has two or more well-separated Type I pulses can be designated as Type I-M (Multiple). Note that one or more of the separate pulses of a Type I-M can be composed of unresolved or overlapping Type I. This is the case for TGF #12, a Type I-M TGF, where pulse #12b shows a partially overlapping peak. Finally, the long duration ($> \sim 1 \text{ ms}$) TGFs, which typically have a softer spectrum, we refer to as “electron TGFs”, or Type E, as it is believed that they are due to an electron-beam, as described by Dwyer, Grefenstette, and Smith (2008); Cohen, et al. (2010) and Briggs et al. (2011). The Type E TGFs observed with Fermi-GBM will be described in more detail in future papers.

7. Summary

We have presented an overview of the temporal characteristics of the first 50 terrestrial gamma-ray flashes (TGFs) that have been observed with the Gamma-Ray Burst Monitor (GBM) on Fermi Gamma-ray Space Telescope (Fermi) during its first 21 months of observations. These data have considerably better temporal resolution and higher efficiency at high energies than have previously been available to the scientific community. More detailed spectral and temporal analysis, beyond that given in this paper

can be derived from the accessible datasets. The unprocessed, raw data used to derive the figures and tables in this paper are publicly available for further study. Access to these data files at the High Energy Astrophysics Science Archive Research Center (HEASARC) at the NASA Goddard Space Flight Center (GSFC), Greenbelt, Maryland, USA, through the ftp site: <http://heasarc.gsfc.nasa.gov/docs/archive.html>. Instructions for retrieving and using these data are given in that link. A large suite of software packages is also available at <http://heasarc.gsfc.nasa.gov/docs/software.html>. Another site at the HEASARC, supported with a help desk, can also be used for converting, plotting and analyzing these data files.

Potential uses in the interpretation and modeling of the TGF processes from the observations giving here include: 1) deriving the altitude of origin of TGFs, 2) the transport of TGF photons through the residual atmosphere between their origin and the spacecraft instrument that observes them, and 3) the temporal relationship between the TGFs, lightning-produced sferics, and transient luminescent events (TLEs). TGF temporal properties can be used to discriminate between models of the origin of TGFs and also provide physical properties of the TGF process.

Future papers will describe in detail spectral characteristics of GBM-Fermi TGFs and the an extension of correlations of the absolute timing of them to observations of timing measurements from lightning sferics, such as those published by Inan, et al. (1996) and more recently by Lu et al. (2010), Connaughton, et al. (2010), and Cohen, et al. (2010).

TGFs are the highest energy atmospheric phenomenon known and are of great current interest. It is expected that the Fermi-GBM experiment will continue to provide valuable observational data on TGFs during its planned initial five-years of mission operation. An extended mission beyond those five years is also likely.

Acknowledgements.

The authors are grateful for help from the Fermi-GBM Science and Operations Team. They have also benefited from insightful and knowledgeable comments and suggestions from the two reviewers.

References

Babich, L. P., E. N. Donskoy, and I. M. Kutsyk (2008), Analysis of atmospheric gamma-ray flashes detected in near space with allowance for the transport of photons in the atmosphere, *Sov Phys JETP*, 107(1), 49, doi:[10.1134/S1063776108070042](https://doi.org/10.1134/S1063776108070042).

Babich, L. P., E. N. Donskoy, and R. A. Roussel-Dupré (2007), Study of relativistic electron avalanche enhancement in the atmosphere at low overvoltages due to avalanche bremsstrahlung, *Geomagn Aeron*, 47(4), 515, doi:[10.1134/S0016793207040135](https://doi.org/10.1134/S0016793207040135).

Bissaldi, E. et al. (2009) Ground-based calibration and characterization of the Fermi gamma-ray burst monitor detectors, *Exper. Astron.*, 24, 47.

Briggs, M. S. , et al (2010). First results on terrestrial gamma ray flashes from the Fermi Gamma-ray Burst Monitor *J Geophys Res.*, 115, A07323, doi:10.1029/2009JA015242.

Briggs, M. S., et al. (2011), Electron-positron beams from terrestrial lightning observed with Fermi-GBM, *Geophys. Res. Lett.*, 38, L02808, doi:10.1029/2010GL046259.

Carlson, B. E., N. G. Lehtinen, and U. S. Inan (2007), Constraints on terrestrial gamma ray flash production from satellite observation, *Geophys. Res. Lett.*, 34, L08809, doi:10.1029/2006GL029229.

Carlson, B. E., N. G. Lehtinen, and U. S. Inan (2008), Runaway relativistic electron avalanche seeding in the Earth's atmosphere, *J Geophys Res*, 113, A10307, doi:[10.1029/2008JA013210](https://doi.org/10.1029/2008JA013210).

Carlson, B. E., N. G. Lehtinen, and U. S. Inan (2010), Terrestrial gamma ray flash production by active lightning leader channels, *J. Geophys. Res.*, 115, A10324, doi:10.1029/2010JA015647.

Chang, B., and C. Price (1995), Can gamma radiations be produced in the electrical environment above thunderstorms?, *Geophys. Res. Lett.*, 22, 1117–1120.[AGU]

Christian, H.J. et al. (2003) Global frequency and distribution of lightning as observed from space by the Optical Transient Detector, *J. Geophys. Res.* **108**, p. 4005 [10.1029/2002JD002347](https://doi.org/10.1029/2002JD002347)..

Cohen, M. B., R. K. Said, U. S. Inan, M. S. Briggs, G. Fishman, V. Connaughton, and S. A. Cummer (2010), A lightning discharge producing a beam of relativistic electrons into space, *Geophys. Res. Lett.*, 37, L18806, doi:10.1029/2010GL044481.

Connaughton, V., et al. (2010), Associations between Fermi-GBM terrestrial gamma-ray flashes and sferics from the World Wide Lightning Location Network, *J. Geophys. Res.*, 115, A12307, doi:10.1029/2010JA015681.

Cummer, S. A., Y. Zhai, W. Hu, D. M. Smith, L. I. Lopez, and M. A. Stanley (2005), Measurements and implications of the relationship between lightning and terrestrial gamma ray flashes, *Geophys. Res. Lett.*, 32, L08811, doi:10.1029/2005GL022778.

Dwyer, J. R., B. W. Grefenstette, and D. M. Smith (2008), High-energy electron beams launched into space by thunderstorms, *Geophys. Res. Lett.*, 35, L02815, doi:10.1029/2007GL032430.

Dwyer, J. R. (2004), A ground level gamma-ray burst observed in association with rocket-triggered lightning, *Geophys Res Lett*, 31, L05119, doi:[10.1029/2003GL018771](https://doi.org/10.1029/2003GL018771).

Dwyer, J. R. (2008), Source mechanisms of terrestrial gamma-ray flashes, *J Geophys Res*, 113, D10103, doi:[10.1029/2007JD009248](https://doi.org/10.1029/2007JD009248).

Dwyer, J. R., and D. M. Smith (2005), A comparison between Monte Carlo simulations of runaway breakdown and terrestrial gamma-ray flash observations, *Geophys Res Lett*, 32, L22804, doi:[10.1029/2005GL023848](https://doi.org/10.1029/2005GL023848).

Fishman, G. J., P. N. Bhat, R. Mallozzi, J. M. Horack, T. Koshut, C. Kouveliotou, G. N. Pendleton, C. A. Meegan, R. B. Wilson, W. S. Paciesas, S. J. Goodman, and H. Christian (1994), Discovery of intense gamma-ray flashes of atmospheric origin, *Science*, *264*, 1313–1316.

Fuschino, F., et al. (2009), AGILE view of TGFs, in *Coupling of Thunderstorms and Lightning to Near-Earth*, *AIP Conf. Proc.* *1118*, N.B. Crosby, T.Y. Huang and M.J. Rycroft, eds, p. 46.

Gjesteland, T., N. Østgaard, P. H. Connell, J. Stadsnes, and G. J. Fishman (2010), Effects of dead time losses on terrestrial gamma ray flash measurements with the Burst and Transient Source Experiment, *J. Geophys. Res.*, *115*, A00E21, doi:10.1029/2009JA014578.

Grefenstette, B. W., D. M. Smith, B. J. Hazelton, and L. I. Lopez (2009), First RHESSI terrestrial gamma-ray flash catalog, *J. Geophys. Res.*, *114*, A02314.

Grefenstette, B. W., D. M. Smith, J. R. Dwyer, and G. J. Fishman (2008), Time evolution of terrestrial gamma ray flashes, *Geophys. Res. Lett.*, *35*, L06802.

Gurevich, A. V. and K. P. Zybin (2005) Runaway Breakdown and the Mysteries of Lightning, *Physics Today* 37-43.

Gurevich, A. V., G. M. Milikh, and R. Roussel-Dupré (1992), Runaway electron mechanism for air breakdown and preconditioning during a thunderstorm, *Phys. Lett. A*, 165, 463–468.[CrossRef]

Gurevich, A. V., K. P. Zybin, and R. A. Roussel-Dupre (1999), Lightning initiation by simultaneous effect of runaway breakdown and cosmic ray showers, *Phys. Lett. A*, 254, 79–97.

Gurevich, A. V., K. P. Zybin, and Y. V. Medvedev (2007), Runaway breakdown in strong electric field as a source of terrestrial gamma flashes and gamma bursts in lightning leader steps, *Phys. Lett. A*, 361(1–2), 119–125.[CrossRef]

Gurevich, A.V., A.N. Karashtin, A.P. Chubenko, L.M. Duncan, V.A. Ryabov, et al. (2004), Experimental evidence of giant electron–gamma bursts generated by extensive atmospheric showers in thunderclouds, *Phys. Lett. A*, 325 389–402.

Inan, U. S., S. C. Reising, G. J. Fishman, and J. M. Horack (1996), On the association of terrestrial gamma-ray bursts with lightning and implications for sprites, *Geophys. Res. Lett.*, 23(9), 1017-1020

Inan, U. S., and N. G. Lehtinen (2005), Production of terrestrial gamma-ray flashes by an electromagnetic pulse from a lightning return stroke, *Geophys. Res. Lett.*, 32, L19818, doi:10.1029/2005GL023702.

Inan, U. S., M. B. Cohen, R. K. Said, D. M. Smith, and L. I. Lopez (2006), Terrestrial gamma ray flashes and lightning discharges, *Geophys Res Lett*, 33, L18802, doi:[10.1029/2006GL027085](https://doi.org/10.1029/2006GL027085).

Lehtinen, N. G., M. Walt, U. S. Inan, T. F. Bell, and V. P. Pasko (1996), γ -ray emission produced by a relativistic beam of runaway electrons accelerated by quasi-electrostatic thundercloud fields, *Geophys. Res. Lett.*, 23, 2645–2648.

Lehtinen, N. G., T. F. Bell, and U. S. Inan (1999), Monte Carlo simulation of runaway MeV electron breakdown with application to red sprites and terrestrial gamma ray flashes, *J. Geophys. Res.*, 104, 24,699–24,712

Lu, G., et al. (2010), Lightning mapping observation of a terrestrial gamma-ray flash, *Geophys. Res. Lett.*, 37, L11806, doi:10.1029/2010GL043494.

Marisaldi, M., et al. (2010a), Detection of terrestrial gamma ray flashes up to 40 MeV by the AGILE satellite, *J. Geophys. Res.*, 115, A00E13, doi:10.1029/2009JA014502.

Marisaldi, M. et al. (2010b), Gamma-ray Localization of Terrestrial Gamma-ray Flashes, *Phys. Rev. Lett.*, 105, 128501.

Meegan, C. A. et al. (2009), The Fermi Gamma-Ray Burst Monitor, *Astrophys. J.*, 702, 791-804.

Milikh, G. M., P. N. Guzdar, and A. S. Sharma (2005), Gamma ray flashes due to plasma processes in the atmosphere: Role of whistler waves, *J. Geophys. Res.*, 110, A02308.

Nemiroff, R., J. Bonnell, and J. Norris (1997), Temporal and spectral characteristics of terrestrial gamma flashes, *J. Geophys. Res.*, 102(A5), 9659-9665.

Østgaard, N., T. Gjesteland, J. Stadsnes, P. H. Connell, and B. Carlson (2008), Production altitude and time delays of the terrestrial gamma flashes: Revisiting the Burst and Transient Source Experiment spectra, *J. Geophys. Res.*, 113, A02307.

Roussel-Dupré, R. A., and A. V. Gurevich (1996), On runaway breakdown and upward propagating discharges, *J. Geophys. Res.*, 101, 2297–2312.

Roussel-Dupré, R. A., E. Symbalisty, Y. Taranenko, and V. Yukhimuk (1998), Simulations of high-altitude discharges initiated by runaway breakdown, *J. Atmos. Sol. Terr. Phys.*, 60, 917–940.[\[CrossRef\]](#)

Shao, X. M., T. Hamlin, and D. M. Smith (2010), A closer examination of terrestrial gamma-ray-flash related lightning processes, *J. Geophys. Res.*, 115, A00E30, doi:10.1029/2009JA014835.

Smith, D. M., L. I. Lopez, R. P. Lin, and C. P. Barrington-Leigh (2005), Terrestrial gamma-ray flashes observed up to 20 MeV, *Science*, *307*, 1085–1088.

Smith, D. M., B. J. Hazelton, B. W. Grefenstette, J. R. Dwyer, R. H. Holzworth, and E. H. Lay (2010), Terrestrial gamma ray flashes correlated to storm phase and tropopause height, *J. Geophys. Res.*, *115*, A00E49, doi:10.1029/2009JA014853.

Splitt, M. E., S. M. Lazarus, D. Barnes, J. R. Dwyer, H. K. Rassoul, D. M. Smith, B. Hazelton, and B. Grefenstette (2010), Thunderstorm characteristics associated with RHESSI identified terrestrial gamma ray flashes, *J. Geophys. Res.*, *115*, A00E38, doi:10.1029/2009JA014622.

Stanley, M. A., X.-M. Shao, D. M. Smith, L. I. Lopez, M. B. Pongratz, J. D. Harlin, M. Stock, and A. Regan (2006) A link between terrestrial gamma-ray flashes and intracloud lightning discharges, *Geophys. Res. Lett.*, *33*, L06803, doi:10.1029/2005GL025537.

Taranenko, Y. N., and R. Roussel-Dupré (1996), High-altitude discharges and gamma-ray flashes: A manifestation of runaway air breakdown, *Geophys. Res. Lett.*, *23*, 571–574.[AGU]

Tavani, M. et al. (2011), Terrestrial Gamma-Ray Flashes as Powerful Particle Accelerators, *Phys. Rev. Lett.*, *106*, doi:10.1103/2011PRL106.018501.

Williams, E., R. Boldi, J. Bór, G. Sátori, C. Price, E. Greenberg, Y. Takahashi, K. Yamamoto, Y. Matsudo, and Y. Hobara (2006), Lightning flashes conducive to the production and escape of gamma radiation to space, *J Geophys Res*, *111*, D16209, doi:[10.1029/2005JD006447](https://doi.org/10.1029/2005JD006447).

FIGURE CAPTIONS

Figure 1. The date (relative to 2 August 2008) of each of the 50 TGFs in Table 1. The increase in the trigger rate is apparent on 10 November 2009 (Day 465), when the onboard trigger algorithm was changed. The detectors were continuously operational. There are several instances of much larger than expected hiatuses in the detection of TGFs. The cause for this is not known.

Figure 2. A sample of data (150 ms) of individual counts during the time of TGF #7. The vertical scale represents the energy loss of the individual photons interacting in the crystal, mapped into 127 quasi-logarithmic channels. In this and other figures below, the zero time indicates the trigger time, the time at which the burst trigger criteria was recognized onboard the spacecraft (see text). Top: Data from the sum of all twelve NaI detectors. Bottom: Data from the sum of both BGO detectors. The TGF occurs at -10.31 ms. The energy versus channel relationship is determined by means on an on-board look-up-table and is quasi-logarithmic. The approximate energy value is shown on the right-hand scale of both figures above.

Figure 3. Global map of the location of all TGFs shown in Table 1. The circle for each TGF is the location of the spacecraft; the location of the origin of the TGF could not be determined accurately with GBM

data alone. The detectors are not operational in the cross-hatched area due to high background radiation.

Figure 4. A plot of the local solar time of the TGFs, binned at three hours per bin. The increase in number of TGFs in the local afternoon and evening is apparent.

Figures 5a-d. Histograms of count rates, uncorrected for deadtime, for 53 TGF pulses from 50 TGFs (three are double-pulse events) observed by GBM-Fermi in 20.5 months of operation. In these figures, the data from all detectors are summed in order to provide improved statistics. The data also span the entire energy range of both detector types, as described in the text. In all of these figures, the data are binned with the same $10\ \mu\text{s}$ resolution over a time span of 1 ms (100 bins, total). In subsequent figures, TGFs are binned selectively. Here, the $10\ \mu\text{s}$ bin width was chosen as a compromise between good time resolution and minimizing statistical fluctuations. For the five long “electron” pulses, noted in Table 1 (and shown with an asterisk below the TGF number), only the leading edges are shown. The entire pulses of these five are shown in Figure 7.

Figure 6. Nine weak TGF pulses. These are re-binned to $40\ \mu\text{s}$ per bin, rather than $10\ \mu\text{s}$ per bin as in Figure 7, in order to improve the statistics. The horizontal and vertical scales are the same in all plots.

Figure 7. Five long TGFs which are believed to be due to electron beams.

These beams are thought to be produced by electrons from TGF sources on the same geomagnetic field lines as those of the Fermi spacecraft at the time of observation.

Figure 8. Three well-separated, double pulse TGFs, binned over a longer timescale, with the bin size indicated. No counts are apparent above the background between the peaks. Note the differences in scales.

Figure 9. Three TGFs which appear to be composed of overlapping pulses.

About seven other TGFs may also consist of overlapping pulses, but they are less apparent than the three shown above, primarily because their intensities are smaller.

Figure 10. Top: Count rate histograms from the fourteen individual GBM detectors for TGF #1. These histograms are shown with 0.1 ms bins over a time period of 20 ms. Note that for this TGF, only the seven detectors (NaI #0 through NaI #6 and BGO #0) detected this TGF to any significant degree. These detectors were all one side of the spacecraft.. This was the only one of the fifty TGFs in Table 1 that showed this high degree of asymmetry.

Bottom: Count rate histograms from the fourteen individual GBM detectors from TGF #5. Unlike the plot shown for TGF #1 above, for

this TGF there were similar numbers of counts in all detectors of each of the two detector types, independent of their location on the spacecraft. Nearly all of the GBM-observed TGFs are of this type.

Figure 11. The t_{50} duration distribution measure, defined in the text, of the 48 TGF pulses in Table 2 (solid bars). This figure excludes the five long (> 1 ms) electron pulses. The total duration of a TGF pulse is assumed to be \sim twice this value. These t_{50} durations are divided into 11 equal, logarithmically-spaced duration groups, as given in Table 3. The median of the t_{50} distribution is at 0.11 ms. Also plotted are the 38 pulses (cross-hatched data) which exclude the ten possible overlapping pulses described in the text and in the caption of Figure 9. This exclusion reduces the median of the duration distributions by \sim 0.01 ms.

Figure 12. A group of six of the TGFs with the narrowest pulses and fastest risetimes and falltimes. They are binned with 4 μ s resolution. All have widths of \sim 50 μ s to \sim 100 μ s and significant changes (risetimes and/or falltimes) on timescales of \sim 10 μ s to 20 μ s

Table 1. Time and location of TGF Triggers

TGF No.	GBM ID YYMMDD.DDD	Date YYYY MM DD	Trigger Time (UT) HH:MM:SS.SSSSSS	Spacecraft Location			Solar Time	
				E. Long.	Lat.	Alt. (km)	HH:MM	Note
1	080807.357	2008 08 07	08:33:24.191042	253.01	+15.30	557.1	01:20	1
2	080828.449	2008 08 28	10:46:30.271448	87.72	+23.64	546.2	16:36	
3	081001.392	2008 10 01	09:24:44.927230	162.67	+10.47	546.5	20:26	
4	081006.797	2008 10 06	19:08:10.745324	159.70	-12.43	559.4	05:59	
5	081025.691	2008 10 25	16:34:45.557752	26.87	-1.12	565.7	18:38	
6	081113.322	2008 11 13	07:44:04.238298	7.33	+2.89	546.9	08:29	2
7	081123.874	2008 11 23	20:58:42.331554	129.88	-15.94	558.2	05:52	
8	081223.051	2008 12 23	01:13:14.665124	203.33	-16.92	553.7	14:48	3
9	090203.356	2009 02 03	08:32:44.380242	125.87	-16.70	568.8	16:42	3
10	090510.498	2009 05 10	11:57:15.985436	24.08	-5.25	563.3	13:37	1
11	090522.190	2009 05 22	04:33:46.890568	167.12	-19.10	562.5	15:46	3
12	090627.274	2009 06 27	06:34:48.325250	281.80	+8.10	561.3	01:19	2
13	090808.739	2009 08 08	17:44:06.096946	301.06	+3.79	564.9	13:43	3
14	090813.215	2009 08 13	05:10:14.790074	278.29	-2.19	554.8	23:39	1

15	090828.147	2009 08 28	03:31:50.217748	252.85	+22.66	563.0	20:22	3
16	091116.633	2009 11 16	15:12:11.150782	123.11	+3.89	553.7	23:40	4
17	091118.985	2009 11 18	23:38:51.984956	148.83	+0.62	552.5	09:49	
18	091130.219	2009 11 30	05:15:32.980584	132.60	-12.02	558.2	14:17	
19	091130.288	2009 11 30	06:55:03.220904	121.23	-5.88	559.9	15:11	3
20	091211.599	2009 12 11	14:22:49.438494	130.45	-7.62	567.4	23:11	3
21	091213.783	2009 12 13	18:47:28.802632	26.36	+2.26	563.6	20:39	
22	091213.876	2009 12 13	21:01:50.479642	140.61	-15.75	556.5	06:30	
23	091213.945	2009 12 13	22:40:23.106924	126.49	-11.47	554.2	07:12	3
24	091214.495	2009 12 14	11:53:27.829662	31.42	+25.34	544.9	14:04	1
25	091221.677	2009 12 21	16:14:34.970184	20.55	-5.80	553.4	17:39	
26	091224.757	2009 12 24	18:10:21.683796	133.73	-0.88	566.2	03:05	2
27	091227.540	2009 12 27	12:58:12.322114	182.48	-4.59	566.2	01:07	
28	091227.801	2009 12 27	19:13:08.596056	62.25	-15.06	564.4	23:21	
29	100103.431	2010 01 03	10:20:36.169226	142.20	-15.80	552.0	19:45	3
30	100104.563	2010 01 04	13:30:50.233714	110.90	-5.31	552.6	20:49	3
31	100110.328	2010 01 10	07:52:32.506562	133.13	-13.08	549.4	16:38	3
32	100125.883	2010 01 25	21:11:36.123060	24.91	-1.34	549.4	22:39	

33	100129.593	2010 01 29	14:14:28.550726	86.86	+5.10	549.0	19:49	
34	100202.802	2010 02 02	19:14:28.039888	149.34	-9.59	555.4	04:58	
35	100203.793	2010 02 03	19:02:24.710500	129.48	-15.65	552.0	03:26	
36	100207.843	2010 02 07	20:14:26.247782	107.62	-4.02	548.7	03:11	
37	100208.349	2010 02 08	08:22:16.994640	142.33	-14.27	561.8	17:37	
38	100210.761	2010 02 10	18:15:56.550044	116.08	-3.36	547.2	01:46	
39	100214.868	2010 02 14	20:50:29.660198	27.79	-11.43	554.4	22:27	
40	100216.663	2010 02 16	15:55:18.709570	111.50	-0.58	552.0	23:07	
41	100218.518	2010 02 18	12:25:39.133716	139.13	-5.54	558.1	21:28	
42	100223.288	2010 02 23	06:54:24.611804	165.26	-14.09	568.2	17:42	
43	100225.345	2010 02 25	08:16:06.232526	135.66	-11.40	567.9	17:06	
44	100225.374	2010 02 25	08:57:52.545288	283.09	+19.26	544.9	03:37	
45	100226.338	2010 02 26	08:06:58.034852	125.64	-13.28	567.4	16:17	3
46	100303.848	2010 03 03	20:21:15.550106	292.78	+1.79	562.6	20:21	
47	100304.842	2010 03 04	20:12:53.044548	285.36	+0.91	560.8	15:03	
48	100305.806	2010 03 05	19:21:14.389138	124.09	-7.14	552.5	03:26	
49	100327.513	2010 03 27	12:19:24.610698	205.20	-9.80	567.5	01:55	1
50	100331.421	2010 03 31	10:05:34.414486	183.27	-19.08	563.7	22:14	

Notes:

- 1- Long TGF; believed to include mirroring electrons (see text)

- 2- Well-separated, double-pulse TGF

- 3- Likely contains overlapping pulses

- 4- New, more sensitive TGF trigger was initiated on 10 November 2009

Table 2. Properties of 53 TGF pulses (see text for definitions)

TGF No.	Start^a (ms)	Pulse t_{50} (ms)	Counts in t_{50}
1	-10.32	0.96	202
2	-11.52	0.12	200
3	-12.95	0.13	197
4	-0.93	0.11	134
5	-9.70	0.11	191
6a	-1.45	0.07	75
6b	-0.13	0.06	54
7	-10.31	0.07	112
8	-12.20	0.14	176
9	-11.16	0.36	182
10	-2.30	0.90	129
11	-6.40	0.28	163
12a	-21.28	0.56	47
12b	-12.43	0.18	193
13	-13.10	0.17	168
14	-14.76	1.68	301
15	-10.12	0.18	196
16	-2.36	0.20	100
17	-2.35	0.08	123
18	-15.47	0.06	85

19	-10.66	0.26	67
20	-7.56	0.36	55
21	-4.54	0.20	64
22	-4.20	0.07	105
23	-12.23	0.13	206
24	0.64	9.60	868
25	-8.18	0.14	49
26a	-2.21	0.12	38
26b	-0.75	0.06	45
27	-15.56	0.09	115
28	-4.65	0.17	221
29	-1.52	0.18	141
30	-10.84	0.36	67
31	-10.46	0.10	112
32	-12.78	0.13	86
33	-14.33	0.08	70
34	-0.26	0.07	69
35	-13.90	0.20	79
36	-1.23	0.12	147
37	-14.64	0.09	68
38	-0.39	0.09	108
39	-10.92	0.12	103
40	-9.94	0.05	79
41	-1.80	0.08	120
42	-3.37	0.06	70
43	-1.70	0.30	95
44	-1.30	0.09	65

45	-7.88	0.28	74
46	-3.12	0.10	49
47	-10.16	0.10	94
48	-12.41	0.105	101
49	-16.00	2.200	98
50	-14.58	0.12	114

a - Relative to trigger time, as given in Table 1

Table 3. Distribution of TGF pulse durations (t_{50}), not including “electron” TGFs.

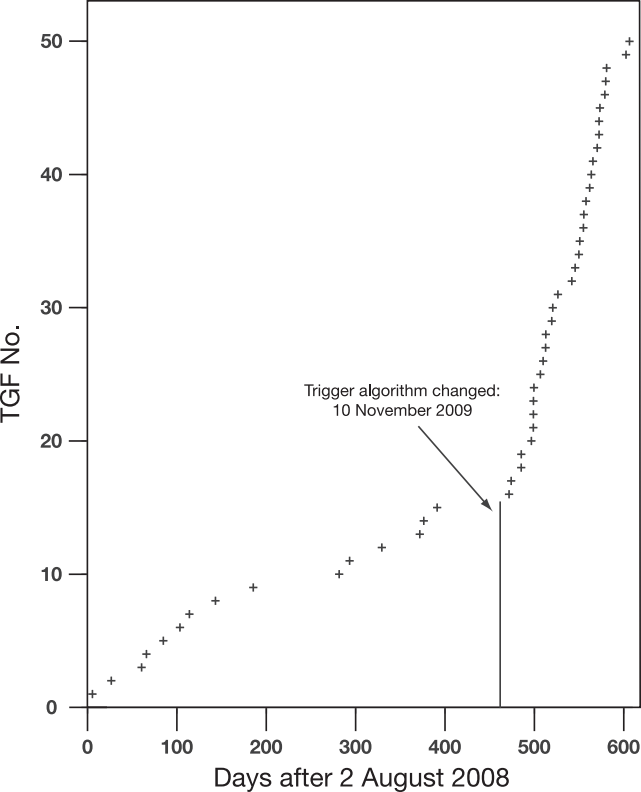
Bin No.	Bin Start (ms)	Bin End (ms)	Bin Mean¹ (ms)	TGFs in Bin²	TGFs in Bin³
1	0.050	0.065	0.057	5	5
2	0.065	0.085	0.074	7	6
3	0.085	0.110	0.096	10	9
4	0.110	0.143	0.125	10	6
5	0.143	0.186	0.163	5	2
6	0.186	0.241	0.212	3	3
7	0.241	0.314	0.275	4	3
8	0.314	0.408	0.358	3	3
9	0.408	0.530	0.465	0	0
10	0.530	0.689	0.604	1	1
11	>0.689	--	--	0	0

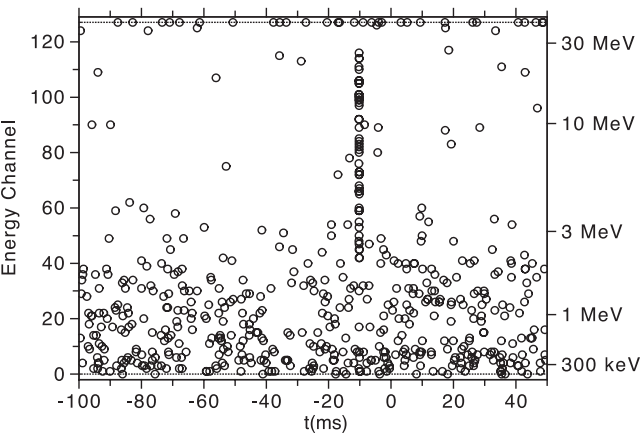
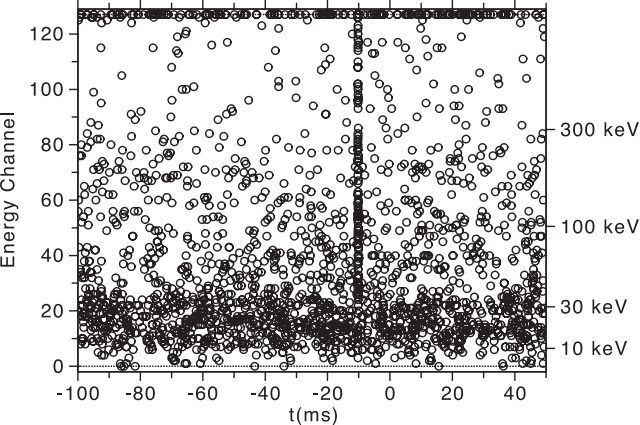
1-

Geometric mean

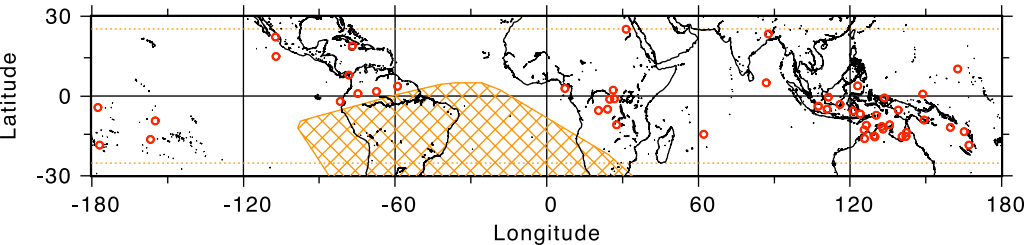
2- All Pulses

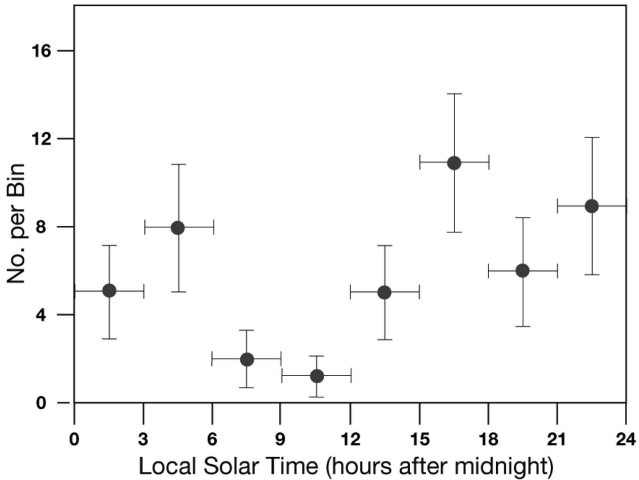
3- Not including pulses that are likely and possibly overlapping



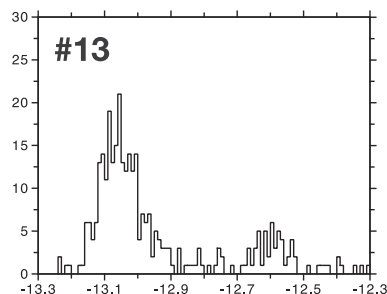
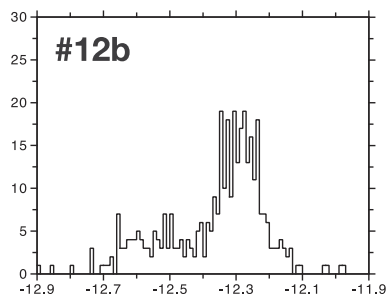
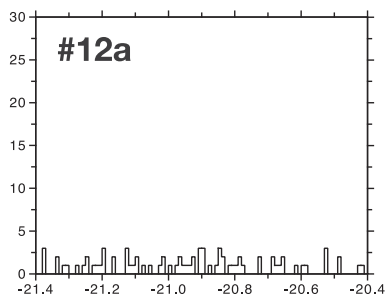
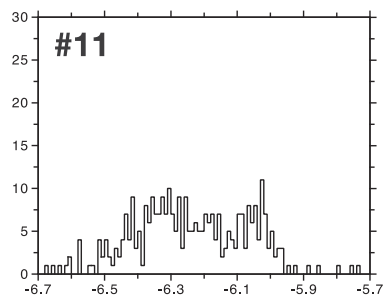
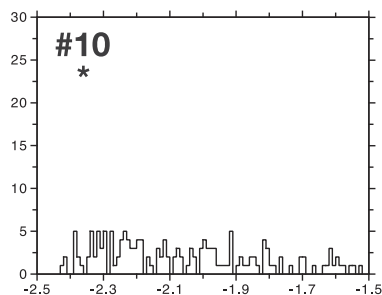
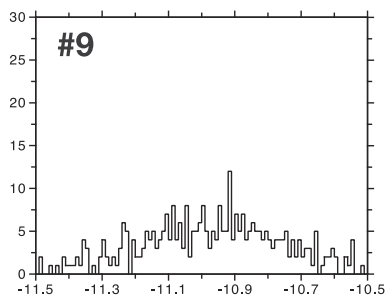
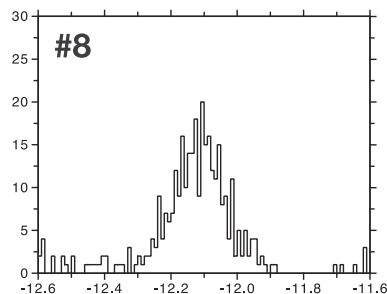
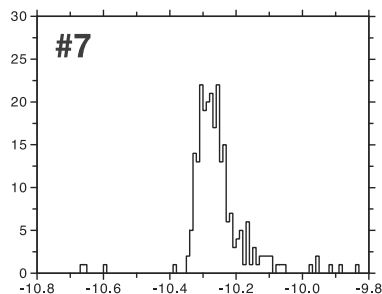
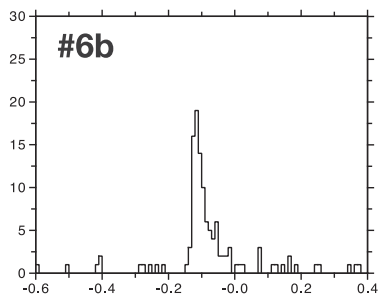
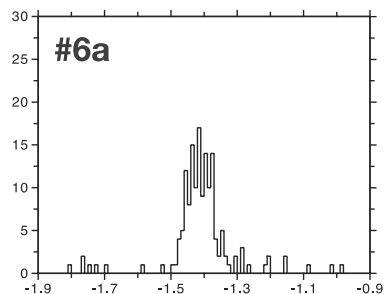
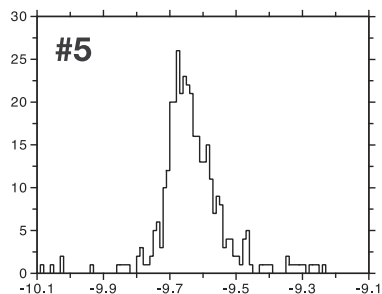
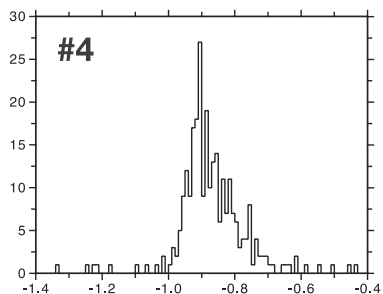
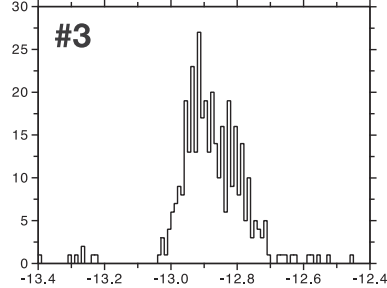
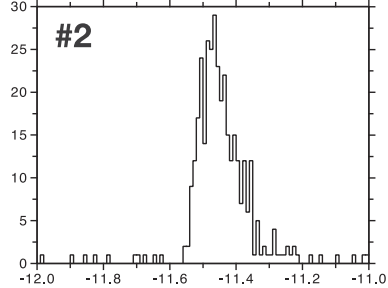
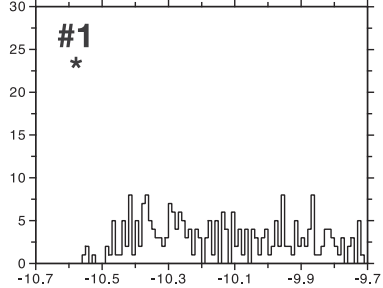


50 GBM TGFs



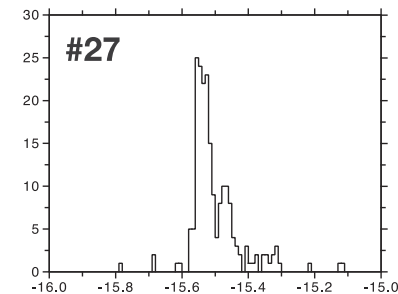
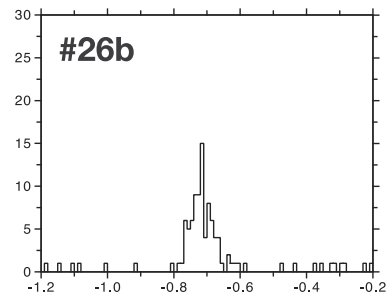
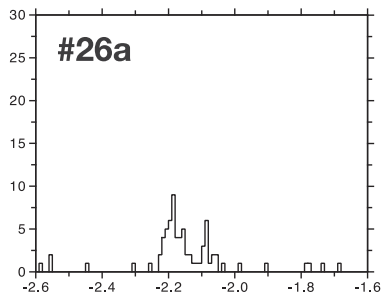
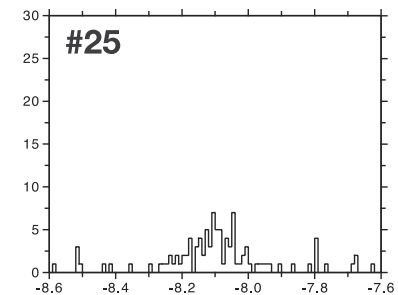
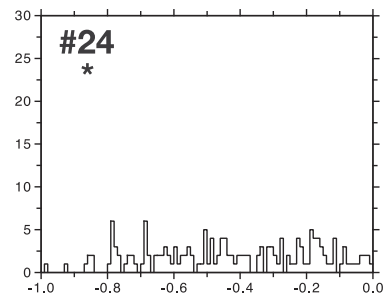
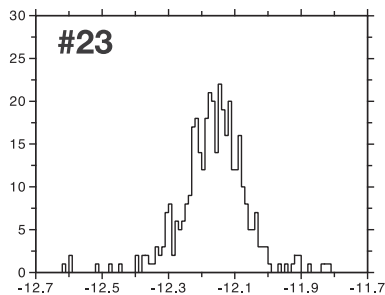
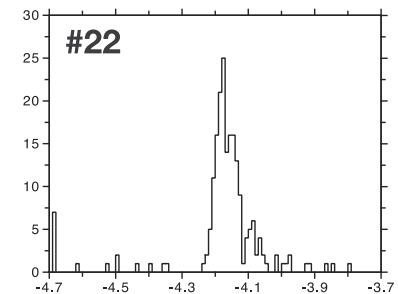
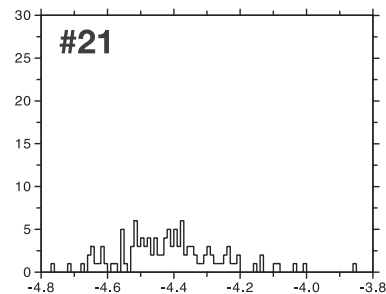
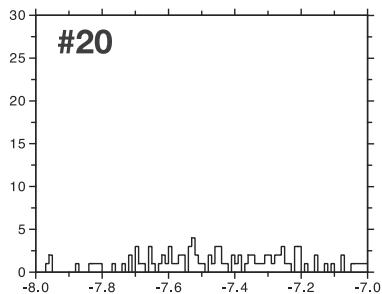
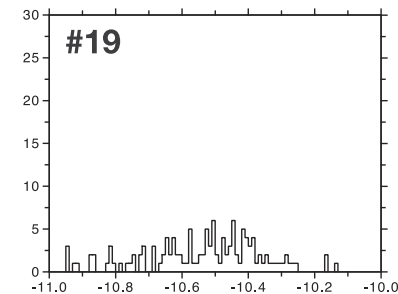
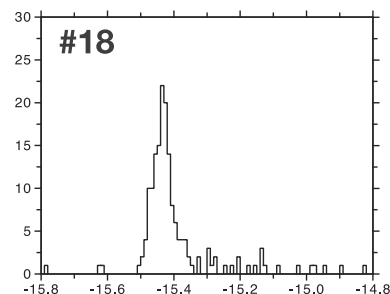
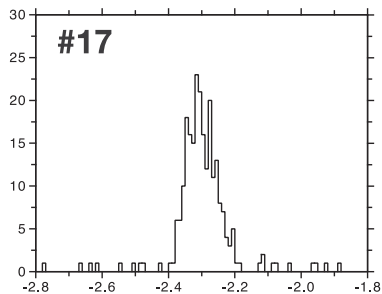
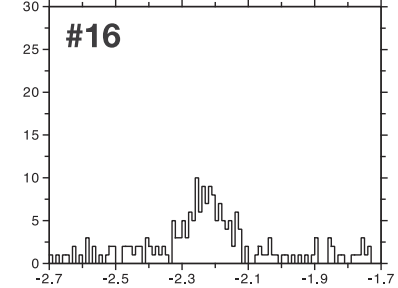
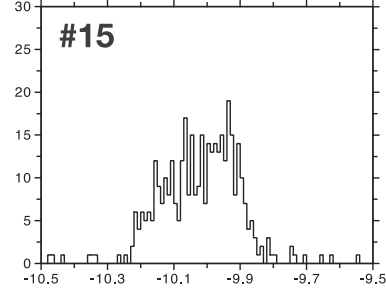
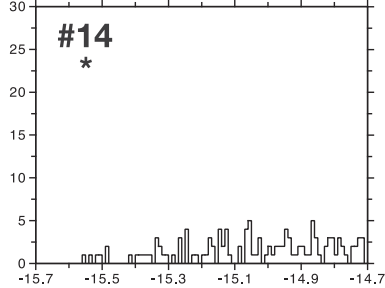


Counts per 10 μ s



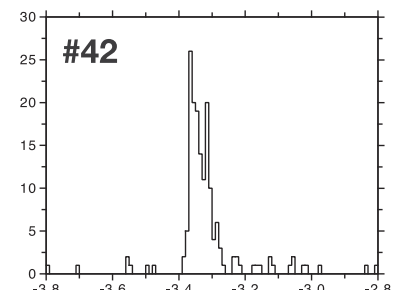
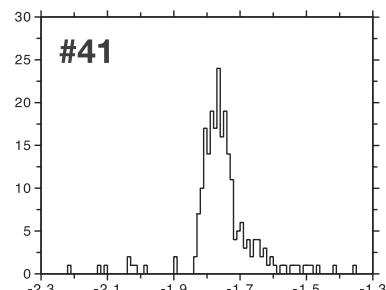
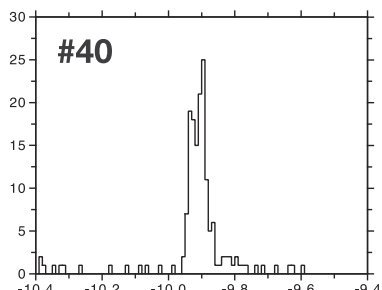
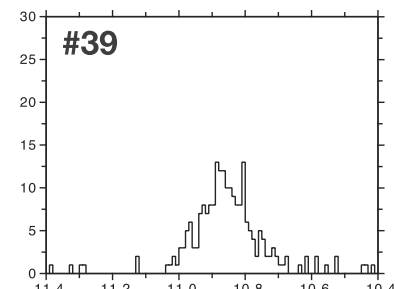
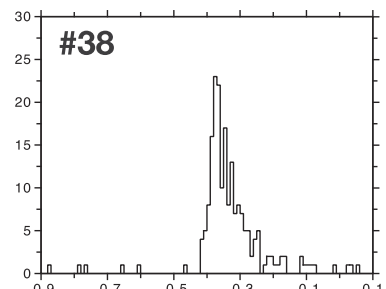
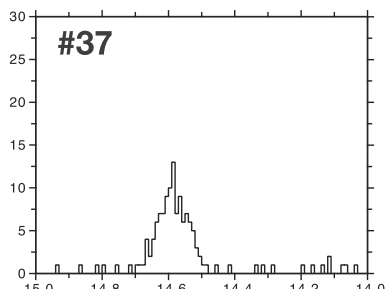
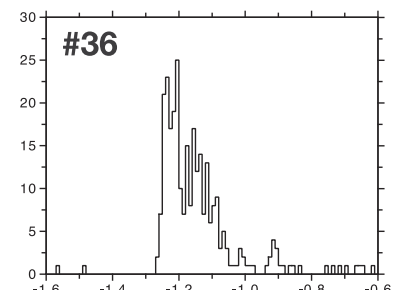
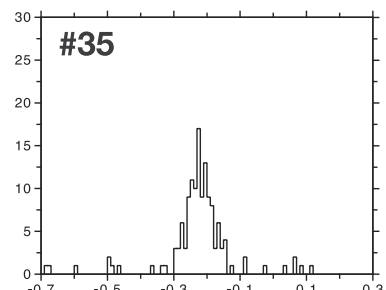
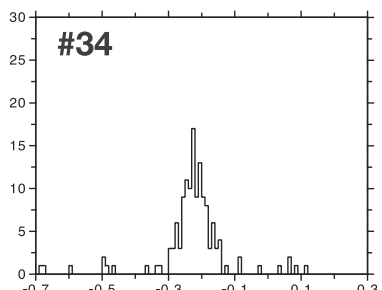
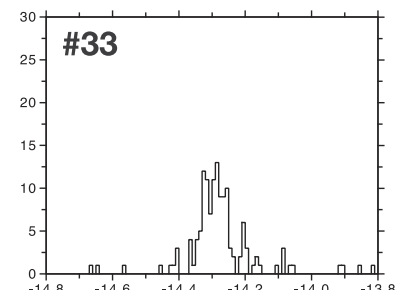
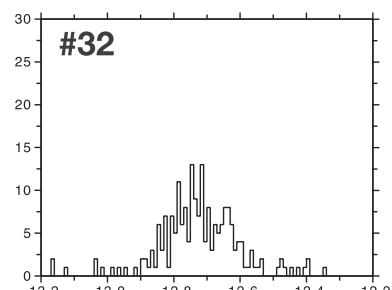
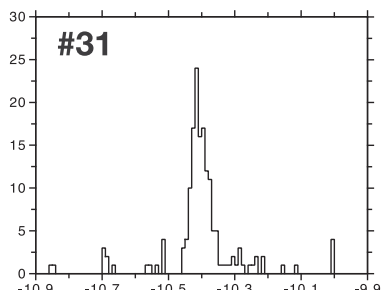
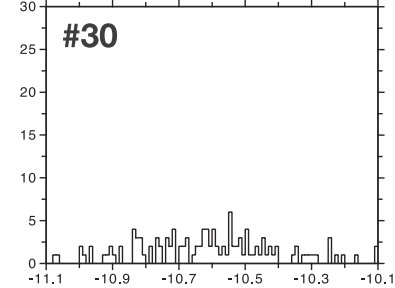
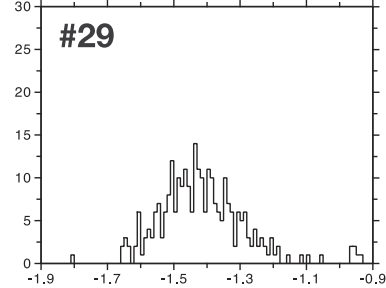
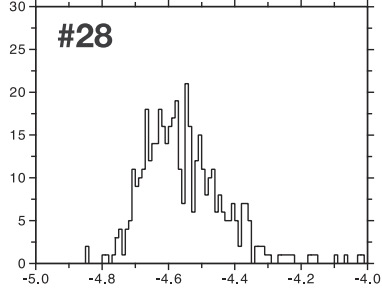
t(ms)

Counts per 10 μ s



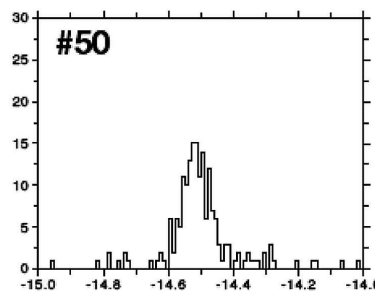
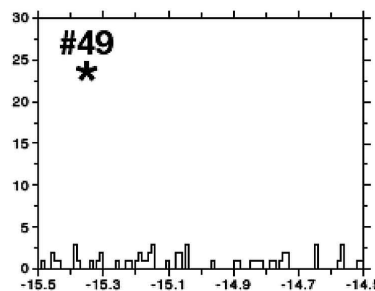
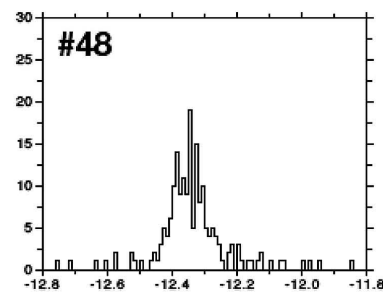
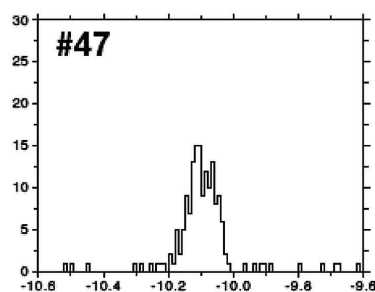
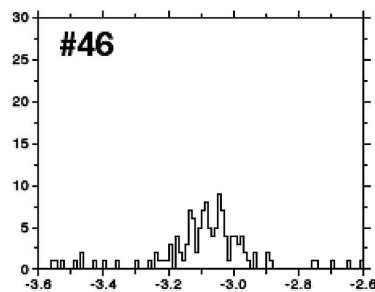
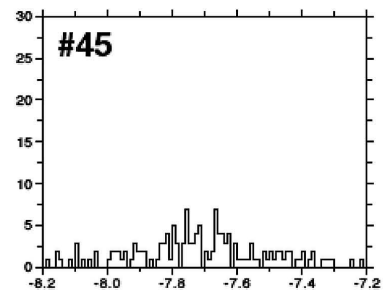
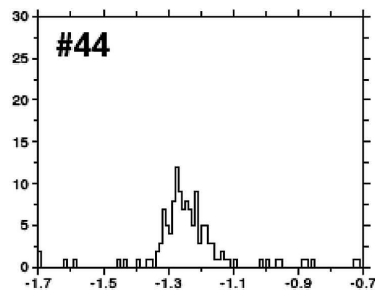
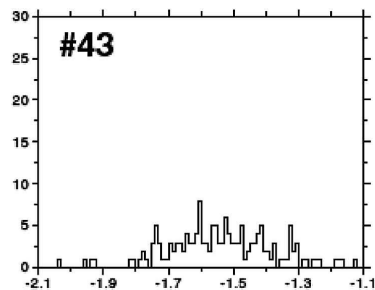
t(ms)

Counts per 10 μ s

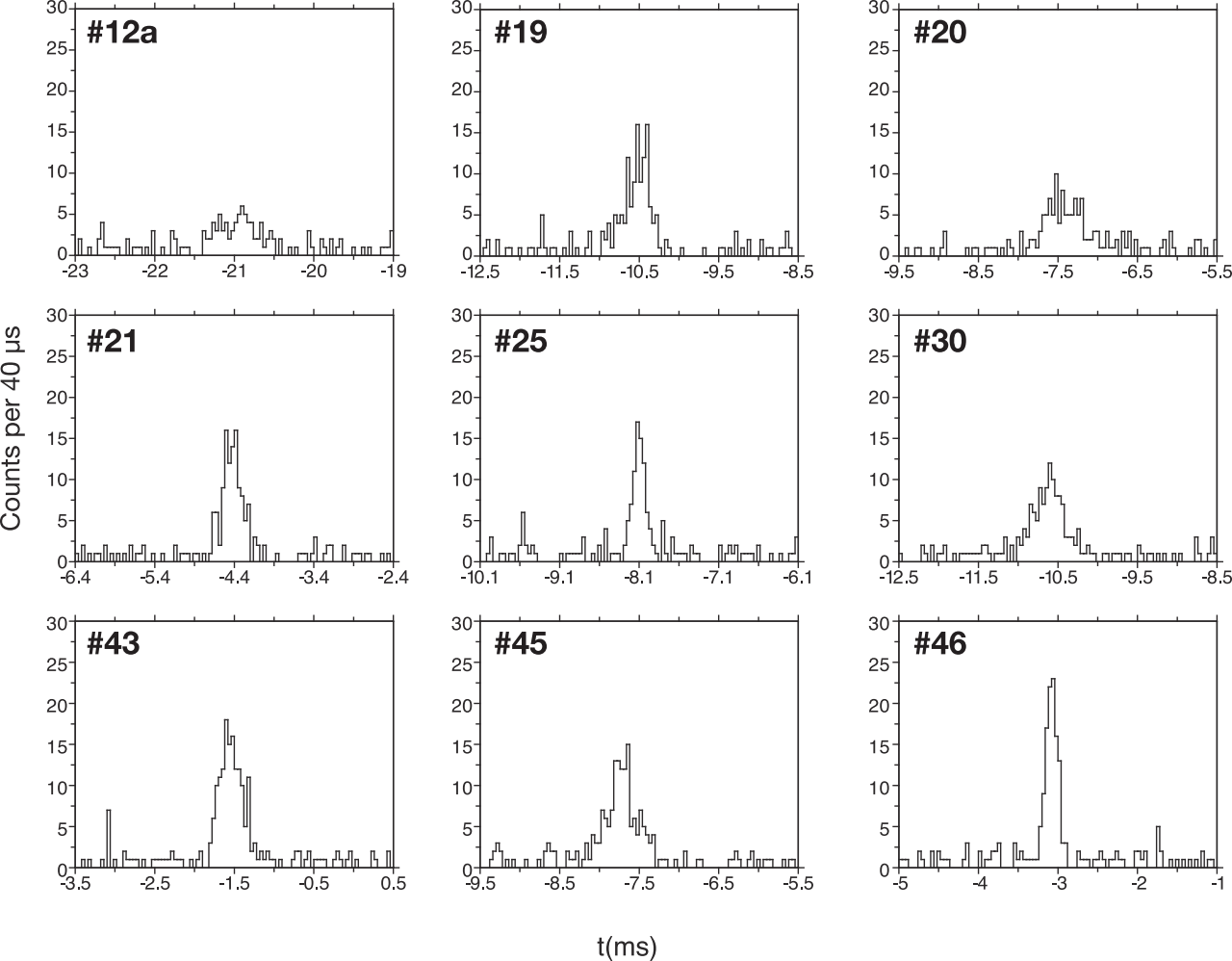


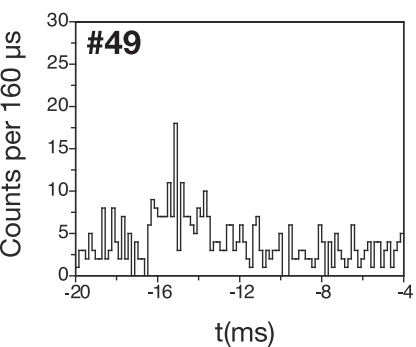
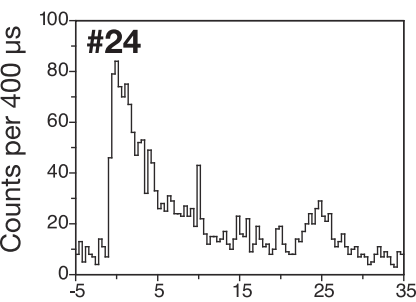
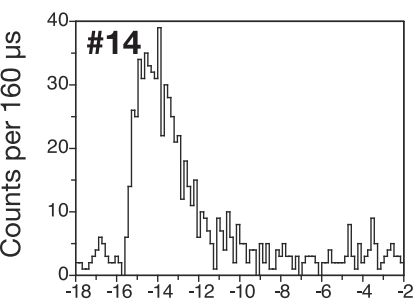
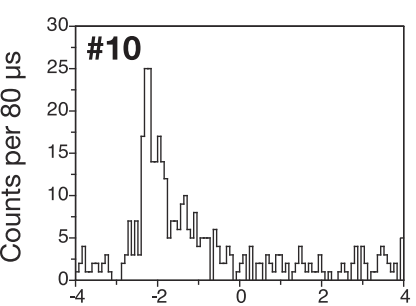
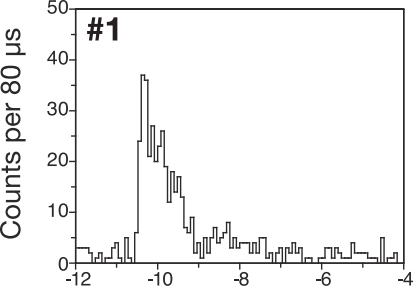
t (ms)

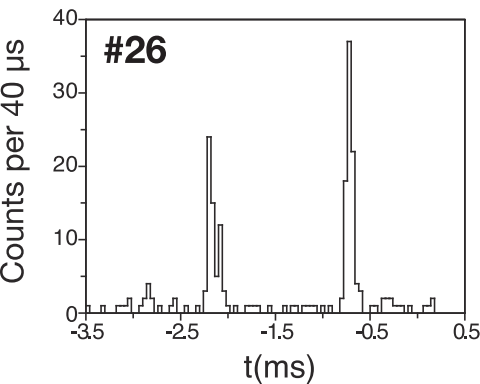
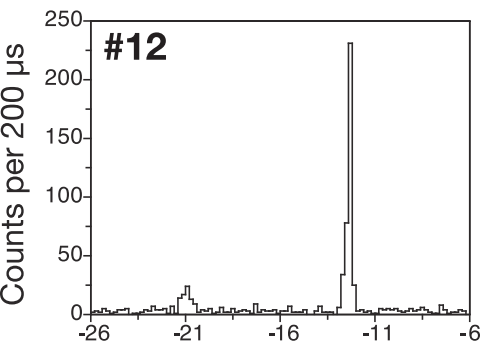
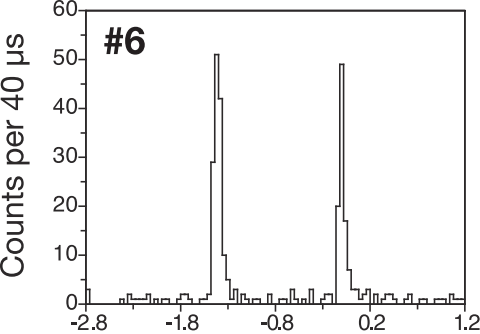
Counts per 10 μ s

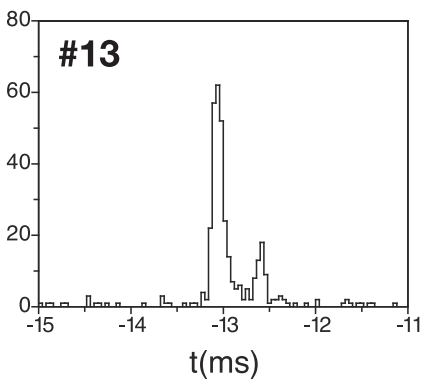
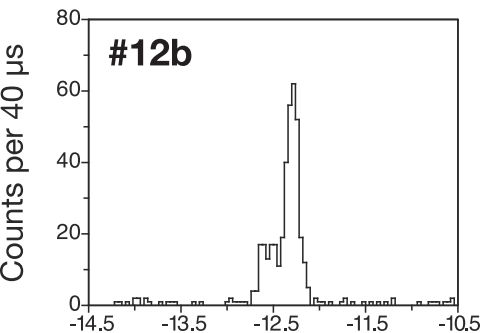
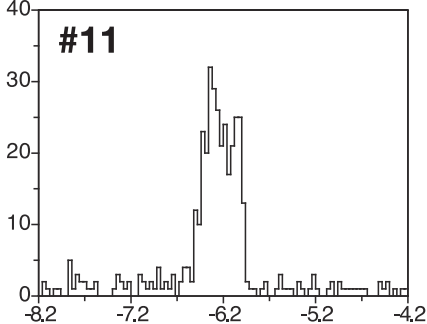


t(ms)

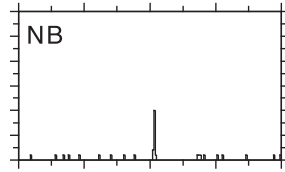
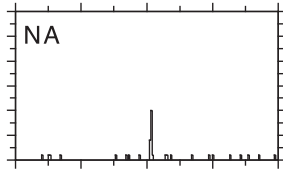
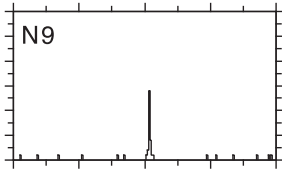
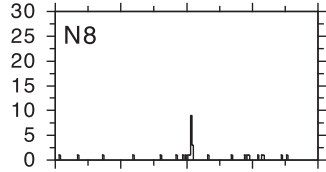
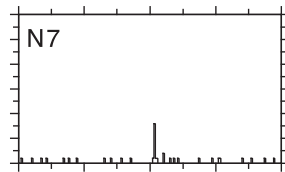
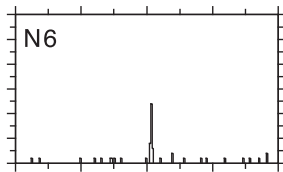
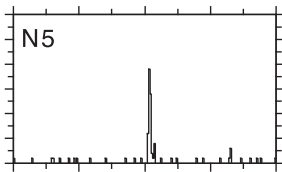
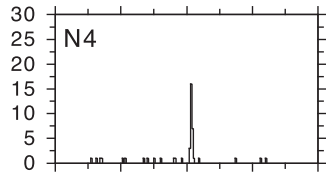
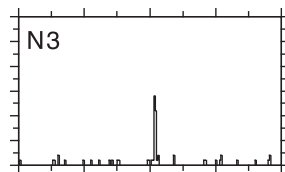
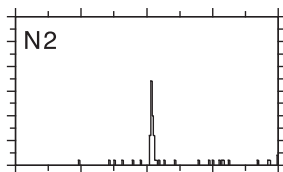
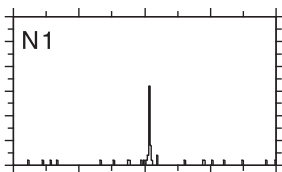
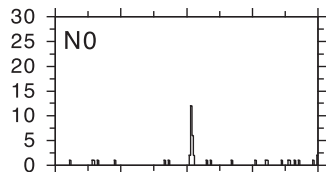
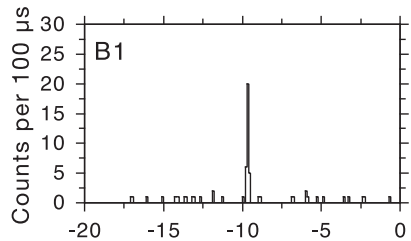
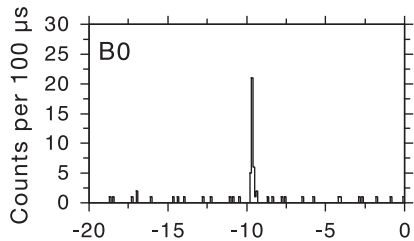








TGF #5 – Separate Detectors



Counts per 100 μ s

t(ms)

